A method for accurate modelling of the crystal response function at a crystal sub-level applied to PET reconstruction

A method for accurate modelling of the crystal response function at a crystal sub-level applied to PET reconstruction

S Stute[1]**, D Benoit**[1]**, A Martineau**[2]**, N S Rehfeld**[1] **and I Buvat**[1]

[1] IMNC Laboratory, UMR 8165 CNRS, Paris 7 and Paris 11 Universities, Orsay, France
[2] Nuclear Medicine Department, Hôpital Saint-Louis, Paris, France

E-mail: stute@imnc.in2p3.fr

Abstract

Positron emission tomography (PET) images suffer from low spatial resolution and signal-to-noise ratio. Accurate modelling of the effects affecting resolution within iterative reconstruction algorithms can improve the trade-off between spatial resolution and signal-to-noise ratio in PET images. In this work, we present an original approach for modelling the resolution loss introduced by physical interactions between and within the crystals of the tomograph and we investigate the impact of such modelling on the quality of the reconstructed images. The proposed model includes two components: modelling of the inter-crystal scattering and penetration (interC) and modelling of the intra-crystal count distribution (intraC). The parameters of the model were obtained using a Monte Carlo simulation of the Philips GEMINI GXL response. Modelling was applied to the raw line-of-response geometric histograms along the four dimensions and introduced in an iterative reconstruction algorithm. The impact of modelling interC, intraC or combined interC and intraC on spatial resolution, contrast recovery and noise was studied using simulated phantoms. The feasibility of modelling interC and intraC in two clinical ^{18}F-NaF scans was also studied. Measurements on Monte Carlo simulated data showed that, without any crystal interaction modelling, the radial spatial resolution in air varied from 5.3 mm FWHM at the centre of the field-of-view (FOV) to 10 mm at 266 mm from the centre. Resolution was improved with interC modelling (from 4.4 mm in the centre to 9.6 mm at the edge), or with intraC modelling only (from 4.8 mm in the centre to 4.3 mm at the edge), and it became stationary across the FOV (4.2 mm FWHM) when combining interC and intraC modelling. This improvement in resolution yielded significant contrast enhancement, e.g. from 65 to 76% and 55.5 to 68% for a 6.35 mm radius sphere with a 3.5 sphere-to-background activity ratio at 55 and 215 mm from the centre of the FOV, respectively, without introducing additional noise. Patient images confirmed the usefulness of interC and intraC modelling for improving spatial resolution

and contrast. Based on Monte Carlo simulated data, we conclude that four-dimensional modelling of the inter- and intra-crystal interactions during the reconstruction process yields a significantly improved contrast to noise ratio and the stationarity of the spatial resolution in the reconstructed images.

(Some figures in this article are in colour only in the electronic version)

1. Introduction

Positron emission tomography (PET) images suffer from low spatial resolution and signal-to-noise ratio, which impair lesion detection and accurate quantification. Spatial resolution could be improved by building PET tomographs with a greater number of smaller crystals. However, this would considerably increase the scanner cost, processing complexity and noise in the measured sinograms. Lengthening the scan duration could increase the signal-to-noise ratio, but the concomitant reduction in patient comfort and daily number of scans is not acceptable. Using image post-smoothing is not satisfactory either, as it reduces image noise at the expense of spatial resolution.

Alternatively, it has been shown that accurate modelling of the phenomena affecting resolution within iterative reconstruction algorithms could significantly improve the spatial resolution and signal-to-noise ratio in the reconstructed PET images (Veklerov *et al* 1988). The model is included in the so-called system matrix (SM) involved in iterative reconstruction. This matrix describes the set of probabilities that a positron emitted in image voxel j be detected in line of response (LOR) i, for all (i, j) pairs. These probabilities depend on many factors, among which are the detector response function (including crystal interactions, defined as the crystal response function—CRF, photomultiplier response and light sharing), the positron range and photon non-collinearity, the geometric effects and the patient-related effects (attenuation, scatter, motion).

Direct calculation of the SM using Monte Carlo simulations has already been performed for a pre-clinical tomograph by Rafecas *et al* (2004). However, even when excluding the animal-related effects, achieving reasonable statistics, hence a robust SM, was extremely challenging. Recently, Ortuño *et al* (2010) used all possible symmetries (including axial translation) to efficiently reduce the number of SM elements to be calculated, thus enabling good statistics and efficient storage of the SM. However, this work was also performed for a small-animal PET device involving less than 10^{13} matrix elements without symmetry. Therefore, comprehensive modelling of the detector response in the SM by direct Monte Carlo calculation is extremely challenging for a currently available clinical tomograph, due to the large number of matrix elements to be stored (between 10^{13} and 10^{16} for a standard clinical PET).

To overcome this issue, several strategies have been proposed. The SM can be expressed as a product of three components (Mumcuoglu *et al* 1996, Qi *et al* 1998): a matrix modelling the blurring effects affecting the projection measurements, a matrix defining the geometrical relationship between the projection space and the image space and a matrix modelling the blurring effects affecting the image. As any blur of the projections results in a blur in the reconstructed image, and any initial blur in the activity distribution (for instance due to the mean-free path of the positron) results in a blur in the projections, this expression of SM yields various options to model the overall resolution loss affecting the imaging process. The resolution loss can thus be modelled in the projection space only (Johnson *et al* 1995,

Mumcuoglu *et al* 1996, Qi *et al* 1998, Selivanov *et al* 2000, Yamaya *et al* 2005, Alessio *et al* 2006, Panin *et al* 2006, Alessio *et al* 2010) or in the image space only (Reader *et al* 2003, Sureau *et al* 2008).

The projection space component can be expressed as a product of sparse matrices, each describing a particular effect, as described by Mumcuoglu *et al* (1996) and Qi *et al* (1998). The drawback is that it can make the reconstruction computationally intensive as many sinogram convolutions are needed. To avoid that, only non-zero matrix elements can be pre-calculated and stored to be later loaded during reconstruction (Johnson *et al* 1995, Selivanov *et al* 2000, Alessio *et al* 2006, Moehrs *et al* 2008), still requiring a large amount of memory. When modelling an overall resolution loss in the image space component only, without explicit decomposition of the various sources of blur, the image estimate is blurred at each iteration before forward projection, using an empirical model, also accounted for in the back-projection process. Although this approach improves spatial resolution, it cannot accurately model angular-dependent crystal blurring effects. Modelling some resolution effects in the projection space and others in the image space (positron range) has also been reported with encouraging results by Rahmim *et al* (2008). However, this work concerned ^{82}Rb, not one of the most common isotopes in PET, the mean range of which (5.9 mm in water) is much larger than that of ^{18}F (0.6 mm in water).

Regardless of the level of modelling (projection and/or image space), the derivation of the blurring parameters can be performed theoretically (Yamaya *et al* 2005, Moehrs *et al* 2008, Rahmim *et al* 2008), empirically (Johnson *et al* 1995, Selivanov *et al* 2000, Reader *et al* 2003) or using Monte Carlo simulations (Veklerov *et al* 1988, Mumcuoglu *et al* 1996, Qi *et al* 1998, Rafecas *et al* 2004, Alessio *et al* 2006, Moehrs *et al* 2008, Ortuño *et al* 2010) or experiments (Panin *et al* 2006, Sureau *et al* 2008, Tohme and Qi 2009, Alessio *et al* 2010).

In previous studies regarding resolution modelling (RM), reconstruction was performed either using sinograms (with projection space and/or image space RM) or using list-mode data (with image space RM only). List-mode data have the advantage of retaining the exact crystal locations for each coincidence but do not allow for grouped LOR manipulations. Raw geometric LOR histograms (LORH) can be defined based on the complete set of all possible geometric LORs, without any distance or angular compression (Kadrmas 2004). Using LORH is thus strictly identical to using list-mode data where all coincidences belonging to the same LOR are grouped and processed simultaneously. So far, in papers related to RM, only Moehrs *et al* (2008) and Alessio *et al* (2010) have used LORH data as the reconstruction input.

This study investigates an original RM approach, in which the blur in resolution introduced by the interactions in the tomograph crystals is estimated using Monte Carlo simulations and modelled in the LORH space along all dimensions. The approach is studied for the Philips GEMINI GXL scanner, and its impact is demonstrated using simulations and clinical images.

2. Materials and methods

2.1. Derivation of the detector response function

The Philips GEMINI GXL is a ring of 28 blocks of 22×29 GSO crystals (4×6 mm^2 respectively in transverse and axial directions, 30 mm in depth) (figure 1(A)). The crystal pitch is 4.3 and 6.3 mm in the transverse and axial directions respectively, and a minimal transaxial distance between two crystals is set to 169 crystals for a coincidence to be validated. The field-of-view (FOV) is 576 mm in transverse and 180 mm in axial directions and the LORH consists of 71 750 756 physical LOR. Considering the geometry of the scanner, a
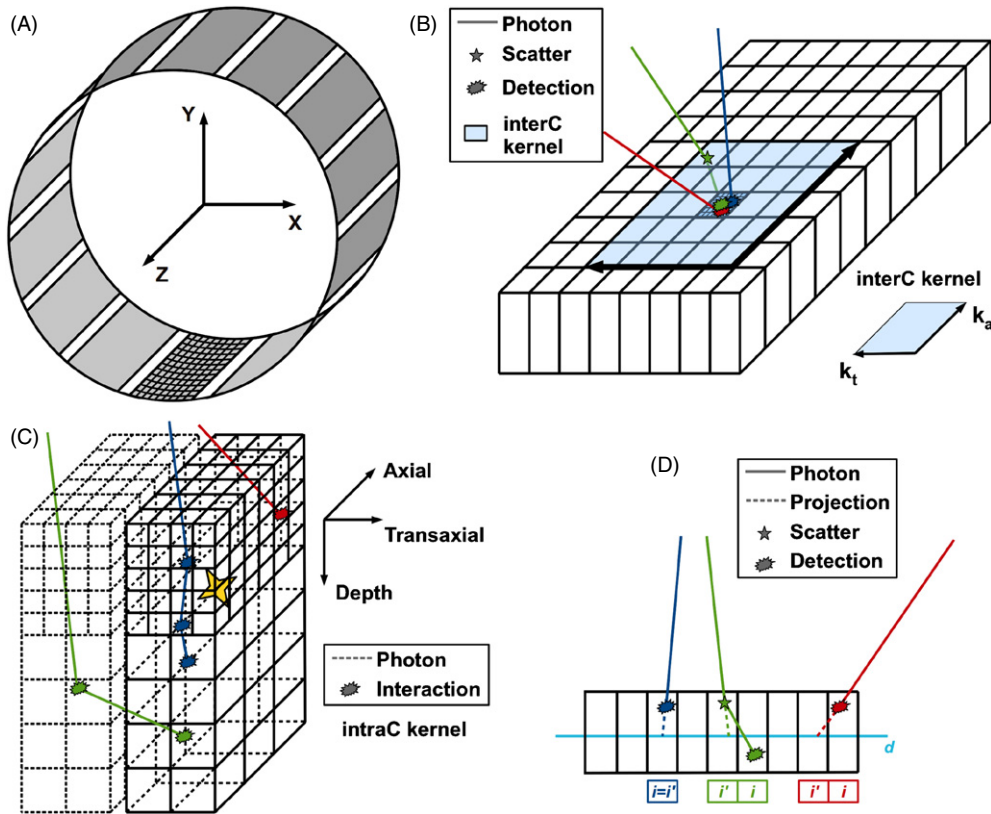
Figure 1. Schematic views of the cylindrical scanner (A), interC kernel at the block level (B), intraC kernel at the crystal level (C) and a 2D view of different effects in the crystals (D). The different coloured tracks represent different photon detection scenarios used to calculate the kernels. The yellow star in C indicates where all detections occurring in the crystal are assigned in usual reconstruction, while our model accounts for the probabilities associated with the different coloured tracks. The green and red tracks in D represent the crystal scattering and penetration effects respectively.

~16-fold symmetry (8 transaxial and 2 axial) can be used to reduce the number of LORs to 4 492 872.

In our model, the detector response function only includes the blur due to interactions in the crystals, and is divided into two components: the inter-crystal scattering and penetration (interC) and the intra-crystal count distribution (intraC). The interC component represents the probability that a photon detected in crystal i (whatever the depth) should have been detected in that crystal at a depth d of interaction (figure 1(D)), blue track) or in a surrounding crystal i' at depth d (figure 1(D), green and red tracks). The intraC component represents the probability that a photon detected in crystal i should have been detected at position $[x_i, y_i, z_i]$ (local Cartesian coordinates) inside this crystal (figure 1(C), blue and red tracks correspond to two different detection positions accounted for in our model while the two are located at the same position in a real PET scanner).

The interC component is represented by a 2D kernel of odd dimensions composed of 4 mm × 6 mm pixels representing crystals (figure 1(B)). It is calculated for a certain depth d

of interaction inside the crystals. The central pixel of the kernel is placed at the location of the crystal in which a signal has been detected. This central pixel thus gives the probability that the actual crystal of detection i is the correct one and has detected the signal at a depth of interaction d. The other pixels of the kernel give the probability for each surrounding crystal i' to be the crystal in which the signal should have been detected at this depth d (figure 1(D), green and red tracks). Considering the GEMINI GXL, 11×15 kernels were calculated considering a given depth d, one for each crystal composing a quarter of a block (22×29 crystals in a block). All blocks were thus supposed to be affected by the same interC effect, as well as the four quarters of each block. An interC kernel positioned near the transaxial border of the block can run over the neighbouring block, so inter-block penetration and scattering effects are taken into account.

The intraC component is represented by a 3D kernel covering the whole crystal (figure 1(C)). Each element of the kernel gives the probability for a signal detected in the crystal to have been detected in this crystal element. Only one kernel was calculated and used for all crystals, assuming all crystals had the same count probability distribution. The interC and intraC components are independent but can be combined.

To calculate the interC and intraC kernels, a Monte Carlo simulation based on a clinical whole-body PET/CT scan was performed using the GATE software (Jan *et al* 2004) and the model of GEMINI GXL (Lamare *et al* 2006). In this simulation, for each photon that produced a signal, its position and direction when leaving the simulated patient were used to project it towards the detector. The crystal i' intersected by this projection at a given depth d gave the ideal position of interaction for this depth d in crystals (figure 1(D)). Knowing this photon was actually detected in crystal i in the Monte Carlo simulation, the interC kernel associated with crystal i and depth d was modified by adding a unit in the pixel associated with crystal i'. In this way, the 11×15 interC kernels were built considering a certain depth d, and normalized so that the sum of all kernel values was 1. To build the intraC kernel, the energy weighted centroid of all intra-crystal interactions in the crystal of detection was recorded for each detected single and a unit was added in the corresponding element of the 3D intraC kernel. After the simulation, the kernel was normalized so that the sum of all kernel values was 1. For these kernels to be smooth, 5 billion signals were recorded.

In the simulations, the interactions of a photon inside the crystals were processed in two steps. First, the crystal in which the highest energy was deposited was taken as the crystal of detection. Second, a unique interaction was determined by calculating the energy centroid of all interactions inside this crystal. This means that the effects of the light readout system, affecting the determination of the detection crystal, were not modelled. This also implies that the interC and intraC kernels only modelled crystal scattering and penetration effects (i.e. the CRF). They both modelled these two effects, but at different levels (i.e. inter- or intra-crystal).

2.2. Reconstruction algorithms

The interC and intraC kernels were used to model the detector response function in the reconstruction. Let k_t and k_a be the transaxial and axial dimensions of the interC kernel (figure 1(B)). For a LOR between two crystals, accounting for the interC component means projecting $k_t^2 \times k_a^2$ rays instead of one. Similarly, if n is the number of elements in the intraC kernel, modelling the intraC component involves projecting n^2 rays instead of one. Modelling both effects results in projecting $k_t^2 \times k_a^2 \times n^2$ rays instead of one. The SMs associated with the two effects separately and in combination were calculated only once and only non-zero values were stored. The Siddon algorithm (Siddon 1985) in its optimized version (Jacobs *et al* 1998) was used to determine the contribution of a ray to the image voxels.

For the intraC model, we empirically chose $n = 300$ with 240 cubic elements (1 mm side) sampling the first centimetre of the crystal depth, and 60 cubic elements (2 mm side) sampling the next 2 cm thickness of the crystal. For the interC kernels, 95.6%, 98.8%, 99.6% and 99.8% of singles were respectively included in kernels of 3×3, 5×5, 7×7 and 9×9 pixels. As the size of the stored SM significantly increases with the interC kernel size, we considered $k_t = k_a = 5$ to build the SM including the interC component only, and $k_t = k_a = 3$ to build the combined matrix including both interC and intraC components. Reconstructed images were $144 \times 144 \times 45$ with cubic voxels of 4 mm side (original sampling of images provided by the manufacturer).

Four SMs, noted M_{GEOM}, M_{intraC}, M_{interC} and M_{CRF}, were considered. M_{GEOM} was built considering only one projected line between the centre of the two crystals defining the LOR, at a depth $d = 9.5$ mm (mean depth of interaction, yellow star in figure 1(D)). M_{intraC} included the intraC component only with $n = 300$. M_{interC} included the interC component only for a depth $d = 9.5$ mm, and using 5×5 kernel size. M_{CRF} combined the intraC component with $n = 300$ and the interC component using 3×3 kernel size. As the intraC kernel had 20 elements in depth, 20 sets of 11×15 interC kernels were built, one for each set of the 20 depths (taken at the mid-depth of an intraC kernel element).

The ordinary-Poisson maximum likelihood expectation maximization (Politte and Snyder 1991) in its ordered-subset form (OP-OSEM) was used by incorporating random and scatter estimates in the denominator during the image update step. Also, weighting for attenuation and normalization (Michel *et al* 1998) was included. The reconstructions were performed considering exact LORs in the LORH space. Details on the SM storage, reconstruction program and computing time are given in the appendix.

2.3. Phantom simulations

2.3.1. Resolution phantom. An acquisition of nine point sources in air was simulated using GATE (Jan *et al* 2004). No attenuation was included and pairs of 511 keV photons in opposite directions were generated (i.e. ignoring positron range and photon-pair non-collinearity). The point sources were aligned parallel to the Y axis and off-centered by 2 mm (i.e. exactly at the centre of a reconstructed voxel). The first point source was placed at $X = 10$ mm (figure 1(A)) and the others were aligned 32 mm apart each. In this way, the last point source was 266 mm away from the transaxial centre of the FOV, i.e. close to the useful FOV edge (288 mm). This simulation was performed at three axial positions: 0, 32 and 64 mm (0 is the axial centre of the FOV). Three million coincidences were recorded per point source (including random coincidences). All coincidences were considered for reconstruction (ten iterations, eight subsets), without correcting for randoms as randoms were less than 1% of the total number of coincidences at this activity concentration (0.25 MBq per point source). Images were reconstructed using each of the four previously described SMs. No correction for scatter nor for attenuation were used since point sources were in air. Also, no correction for variable crystal efficiency was needed since all crystals had the same efficiency in the simulation. Tangential, radial and axial resolutions were estimated for each reconstructed point source by measuring the full-width at half-maximum (FWHM) of the count profiles.

2.3.2. Contrast and noise phantom. Contrast recovery (CR), given by equation (1), as a function of noise was studied using simulations of a water cylindrical phantom (110 mm radius, 190 mm length) parallel to the scanner axis, filled with homogeneous activity. Six water spheres with homogeneous activity were placed in the mid plane of the phantom, with their centres 55 mm from the phantom axis. The radii of the spheres were 6.35, 7.95, 9.55,

12.7, 15.9 and 19 mm and the sphere-to-background activity ratio was 3.5. Two simulations were performed: one with the phantom centred in the transaxial FOV, and another 160 mm off-centred so that the smallest sphere was the farthest from the transaxial FOV centre. Twenty five MBq was inserted in the FOV and 100 million coincidences were recorded for each simulation. As for the point source simulations, pairs of 511 keV photons were generated. Images were reconstructed for each SM, with 50 iterations and 16 subsets. A delayed coincidence window was used for random estimation, and scatter was estimated using a convolution-based method (Bailey and Meikle 1994). Attenuation was corrected using a 4 mm sampled attenuation map of the cylindrical phantom (0.096 cm^{-1} attenuation coefficient). As for the point source simulations, no correction for variable crystal efficiency was needed. For all four reconstructions and for a given number of iterations, we measured the mean activity A_{sph} in the real sphere contours, the mean activity A_{bg} and the standard deviation σ_{bg} in voxels contained in a large background region (excluding the five first and last slices, and at least two voxels away from the cylinder and sphere boundaries). CR and background noise (BN) were calculated as defined in equations (1) and (2):

$$CR = \frac{A_{sph}/A_{bg}}{3.5} \times 100 \tag{1}$$

$$BN = \frac{\sigma_{bg}}{A_{bg}} \times 100. \tag{2}$$

Using this phantom placed at the centre, 40 independent simulations of 30 million coincidences were also performed. Each simulation was corrected and reconstructed using exactly the same processing as for the simulation involving 100 million coincidences. The 40 replicates were used to calculate the covariance for the central pixel in a uniform slice axially located 32 mm off-centre.

2.4. Patients

Two patient studies (P1 and P2) were performed using a clinical Philips GEMINI GXL PET/CT scanner. Patients were injected with ^{18}F-NaF (269 MBq for P1—63 kg—and 289 MBq for P2—92 kg) and scanned 1 h after intravenous injection. CT scanning used a 120 kV tube voltage, rotation time of 0.5 s, beam current of 188 mA for 100 mAs per reconstructed slice, pitch of 0.94, 16×1.5 mm^2 collimation and 5 mm slice thickness reconstruction. In PET, prompts and delay sinograms were collected for 2 min per bed position, and converted into LORH. The crystal efficiency and geometric normalization factors were derived in the LORH space from the correction factors given by the console. Scatter LORH were estimated using Monte Carlo simulations (Holdsworth *et al* 2002). Dead-times were corrected using a single scale factor given by the scanner console for each bed position, derived from the single count rates. Patients were scanned with 19 bed positions. Images were reconstructed using the M_{GEOM} and M_{CRF} SMs and the same OP-OSEM algorithm (8 subsets) as for the contrast phantom, but including weighting for attenuation and normalization (Michel *et al* 1998).

Using M_{GEOM}, images at iteration 5 were considered and post-smoothed using a 3D Gaussian kernel of 4 mm FWHM, to mimic clinical conditions. Using M_{CRF}, images corresponding to iteration 4 were considered without post-smoothing. These parameter settings ensured a similar noise level in the abdomen for the two SMs. As an illustration, images from the original clinical protocol (two iterations of the LOR-RAMLA algorithm (Hu *et al* 2007), relaxation parameter of 0.04, blob radius of 8 mm, blob shape parameter of 4.3363, Bessel function order of 2, and $95 \times 95 \times 33$ blob matrix) were also calculated. LOR-RAMLA
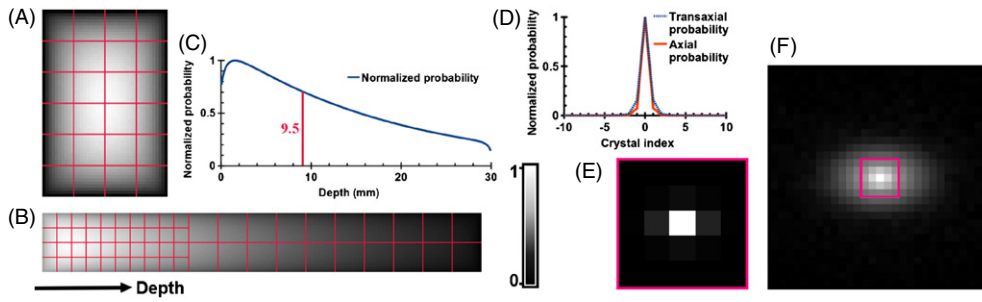
Figure 2. The 3D intraC kernel (A)–(C) and a 2D interC kernel (D)–(F) used to derive the CRF. (A) and (B) are summed projections of the intraC kernel along the depth and along the axial axis of the crystal, respectively (figure 1(C)). (C) The interaction probability along the crystal depth, derived from (B). (E) A 2D 5×5 interC kernel and (F) its logarithm (with 29×29 crystals). (D) The axial and transaxial profiles over the centre of the kernel shown in (E). All grey scales were normalized with minimum at 0 and maximum at 1.

included random coincidence correction using delayed sinogram and scatter correction based on single scatter simulation (Accorsi *et al* 2004) inside the iterative loop (Politte and Snyder 1991), weighted attenuation correction (Michel *et al* 1998), and dead-time correction. LOR-RAMLA used $295 \times 161 \times 841$ sinogram sampling with radial bins aligned with respect to the crystals (considering scanner geometry) and azimuthal angular mashing. The LOR-RAMLA algorithm uses a pre-calculated and stored SM defining geometric relationship between LORs and blobs, using a 16-fold symmetry and axial translation symmetry (Hu *et al* 2007).

3. Results

3.1. Kernels and system matrices

Figures 2(A) and (B) show 2D views of the 3D kernel modelling the intraC component. For illustration purpose, a fine sampling (i.e. cubes of 0.1 mm) of the kernel is used, and the actual sampling used to calculate M_{intraC} is represented in red (sampling of the first cm of the crystal depth in figure 2(A)). Summing all elements corresponding to the same depth (figure 2(B)) gives the interaction probability along the depth of the crystal (figure 2(C)). The median depth of interaction (9.5 mm) is also shown (identical curve integrals on the left and right side of this depth). Figure 2(E) shows an interC 2D 5×5 kernel for a crystal at the centre of a block and for a depth of interaction of 9.5 mm. The logarithm of the interC 2D 29×29 kernel is also shown in figure 2(F), with the border of the actual 5×5 kernel in red. Transaxial and axial profiles over the centre of the interC kernel are plotted in figure 2(D). The profile was broader along the transaxial dimension due to the smaller crystal size (4 mm compared to 6 mm axially). The pixel at the centre contained 67.3% of the total number of singles, 31.7% were distributed in the rest of this 5×5 kernel, and 1.0% were not included in this kernel. Table 1 shows the characteristics of the 4 SMs.

3.2. Simulations

3.2.1. Resolution phantom. The radial, tangential and axial FWHM averaged over the three axial positions are plotted for the nine point sources in figure 3, with associated standard deviations. The radial resolution obtained using M_{GEOM} changes from 5.3 to
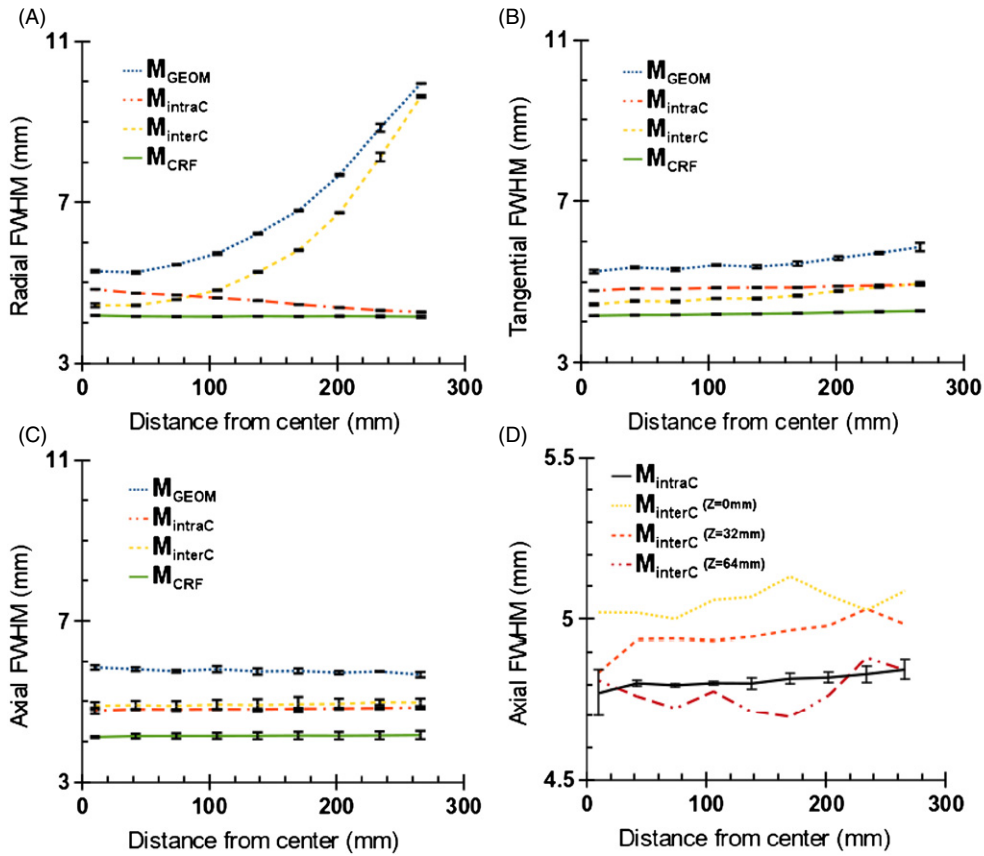
Figure 3. Radial (A), tangential (B) and axial (C) FWHM for the four reconstructions of the point source simulations, averaged over the three axial positions of the point sources. Details for M_{interC} results at each axial position are given in the graph in (D).

Table 1. Characteristics of the four SMs.

System matrix	Size (GB)	Number of rays traced for the system matrix calculation	Minimal number of non-zero voxels in an LOR	Maximal number of non-zero voxels in an LOR	Mean number of non-zero voxels in an LOR
M_{GEOM}	6.5	4.5×10^6	34	325	178
M_{intraC}	46	4.0×10^{11}	288	3212	1478
M_{interC}	175	2.8×10^9	1020	11 176	5184
M_{CRF}	155	2.5×10^{14}	1296	8473	4594

10 mm when moving away from the transaxial FOV centre. M_{interC} shows the same trend, with a systematically improved radial resolution. M_{intraC} yielded an improved radial resolution, varying from 4.8 at the centre to 4.3 mm at the edge. The correction for both intraC and interC effects using M_{CRF} yielded a stationary radial resolution of 4.2 mm FWHM. The tangential resolution was almost stationary across the FOV, varying only from 5.3 to 5.9 mm with M_{GEOM}. Similar stationary tangential resolution was obtained with M_{interC} (~1 mm smaller FWHM
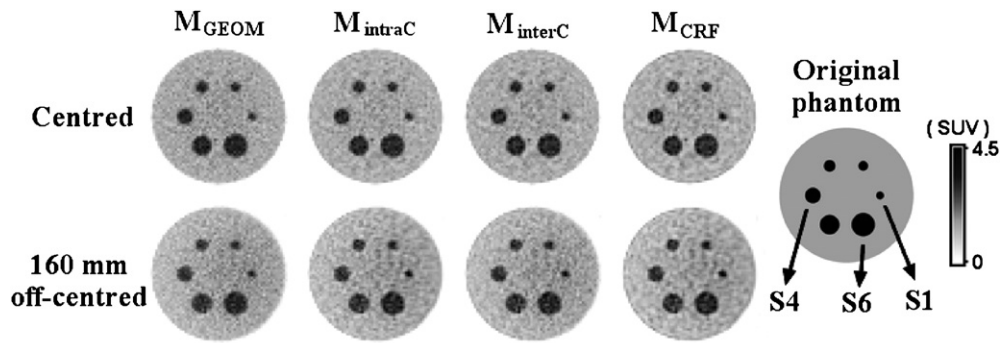
Figure 4. Reconstructed images of the centred and off-centred contrast phantom, using the different SMs. All images have a background noise of 27%. The original phantom giving the simulated activity distribution is also shown. The three spheres associated with arrows are those for which CR is shown in figure 5.

than with M_{GEOM}). Using M_{intraC}, spatial resolution was also stationary at ~4.8 mm. The best tangential stationary resolution was obtained with M_{CRF} (4.2 mm). The axial resolution was stationary whatever the SM. M_{GEOM}, M_{intraC}, M_{interC} and M_{CRF} yielded axial resolutions of 5.8, 5.0, 4.8 and 4.2 mm FWHM respectively. Along this direction, M_{interC} improved resolution slightly less than M_{intraC}, with a larger dependence on the axial position (larger error bars for M_{interC} in figure 3(C). Mean and standard deviation of the M_{intraC} axial FWHM are plotted against the axial FWHM using M_{interC} for each axial position (i.e. 0, 32 and 64 mm) in figure 3(D), showing that the improvement brought by M_{interC} was greater for point sources near the edge of the axial FOV compared to sources centrally located in the axial FOV. Also, for 0 and 32 mm axial positions, the improvement is less than that brought by M_{intraC}.

3.2.2. Contrast and noise phantom. Figure 4 shows the contrast phantom images obtained using the different SMs at a same value of BN (27%), for the centred and off-centred phantoms. The corresponding iteration numbers for the centred phantom are 8, 9, 10 and 15 for reconstructions using M_{GEOM}, M_{intraC}, M_{interC} and M_{CRF} respectively (8, 13, 10 and 17 for the off-centred phantom). The simulated activity distribution is also shown as a reference.

Figure 5 shows the trade-off between CR and BN for all reconstructions, for both centred and off-centred phantoms. Results for the 6.35 (S_1), 9.55 (S_4) and 19 (S_6) mm radius spheres are plotted. Considering the centred phantom, for a given level of noise, M_{intraC} improved CR compared to M_{GEOM}. M_{interC} improved CR more than M_{intraC}, and the best CR was obtained using M_{CRF}. This is in agreement with the point source measurements made at a distance of 55 mm from the transaxial FOV centre (figure 3). However, for the off-centred phantom, the smallest sphere S_1 was at 215 mm from the FOV centre. In this case, M_{intraC} gave a better CR compared to M_{interC}, unlike what was observed for the centered phantom. The same observation, but less pronounced, can be made for the sphere S_6, that was a bit closer to the FOV centre in the off-centred phantom. For the sphere S_4, the closest to the FOV centre, M_{interC} gave a better CR than M_{intraC}, as for any sphere of the centred phantom. These observations are all in agreement with the point source observations at each considered distance from the FOV centre (figure 3).

For any reconstruction and any sphere, the CR was poorer for the off-centred phantom than for the centred one. At the level of noise (36.5%) reached by M_{GEOM} reconstruction
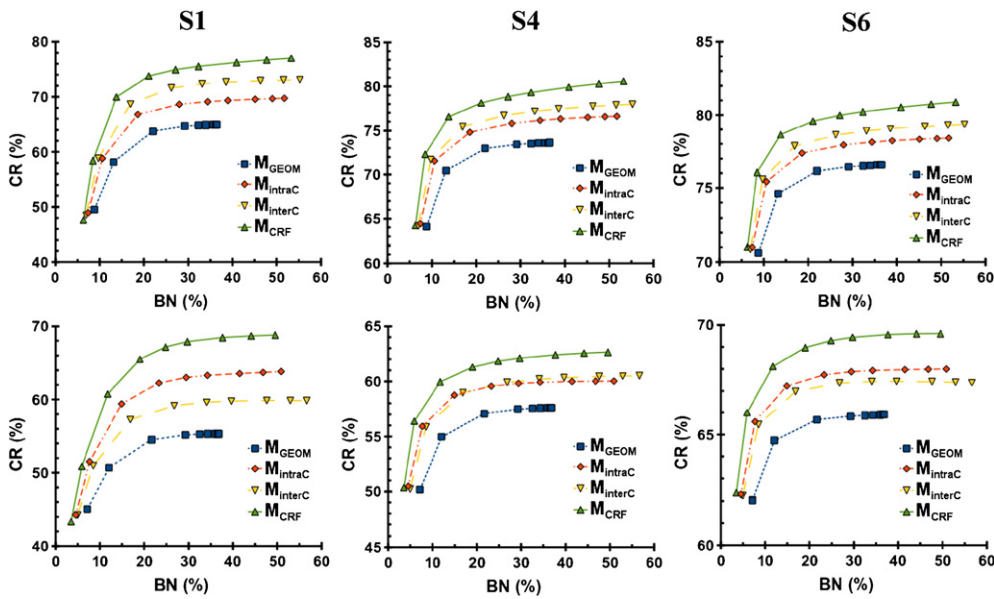
Figure 5. CR versus BN curves for the centred (upper row) and off-centred (lower row) phantom, and for the four different reconstructions. S_1, S_4 and S_6 are the 6.35, 9.55 and 19 mm radius spheres, respectively. Iteration numbers shown by the symbols from left to right are 1, 2, 5, 10, 15, 20, 30, 40 and 50.

for its best CR (for both centred and off-centred phantoms), the CR for the S_1 sphere were about 65, 69, 72.5 and 76% for the M_{GEOM}, M_{intraC}, M_{interC} and M_{CRF} respectively for the centred phantom. These CR were 55.5, 63.5, 59.5 and 68% for the off-centred phantom. The CR improvement was the highest for the smallest sphere as partial volume effect is greater for small objects. Convergence of the reconstructions modelling physical effects was slower than for M_{GEOM}, and M_{CRF} converged even more slowly than M_{intraC} and M_{interC}. For both phantoms, at iteration 5, any of these reconstructions already achieved better CR than the M_{GEOM} reconstruction could ever reach.

Figure 6 shows the covariance profiles obtained for a voxel at the centre of the transaxial FOV and along the X axis. The covariance was compared at a given resolution (figure 6(A)), at a given iteration (iteration 10 in figure 6(B)), and for images with the same amplitude of BR (figure 6(C)). When accounting for detector blurring effects, the peak of covariance was reduced (also observed in figures 4 and 5) with less negative values. Figure 6(C) shows that the width of the peak slightly increased when modelling the detector response, which explains why in figure 4 images at the same noise level (defined by BN) showed different noise textures.

3.3. Patient images

Figure 7 shows coronal slices for P1 and P2 for each reconstruction method. All images have approximately the same level of noise in the abdomen. Images from M_{CRF} showed improved resolution compared to those from M_{GEOM}, particularly along the spine. An improvement compared to LOR-RAMLA was also observed. To the best of our knowledge, the LOR-RAMLA algorithm does not include more details regarding the modelling of the detector response than M_{GEOM}, except that it is a blob-based algorithm that somehow intrinsically
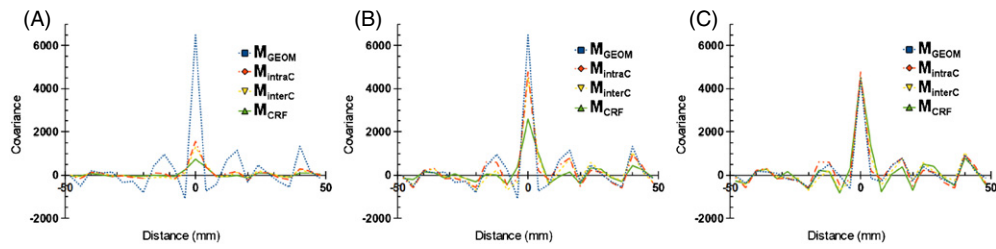
Figure 6. Covariance profiles observed for the four reconstructions, for a voxel at the centre of the transaxial FOV and along the *X* axis, at (A) equal resolution for the smallest sphere, (B) equal iteration and (C) equal variance. These graphs were obtained for the centred phantom.
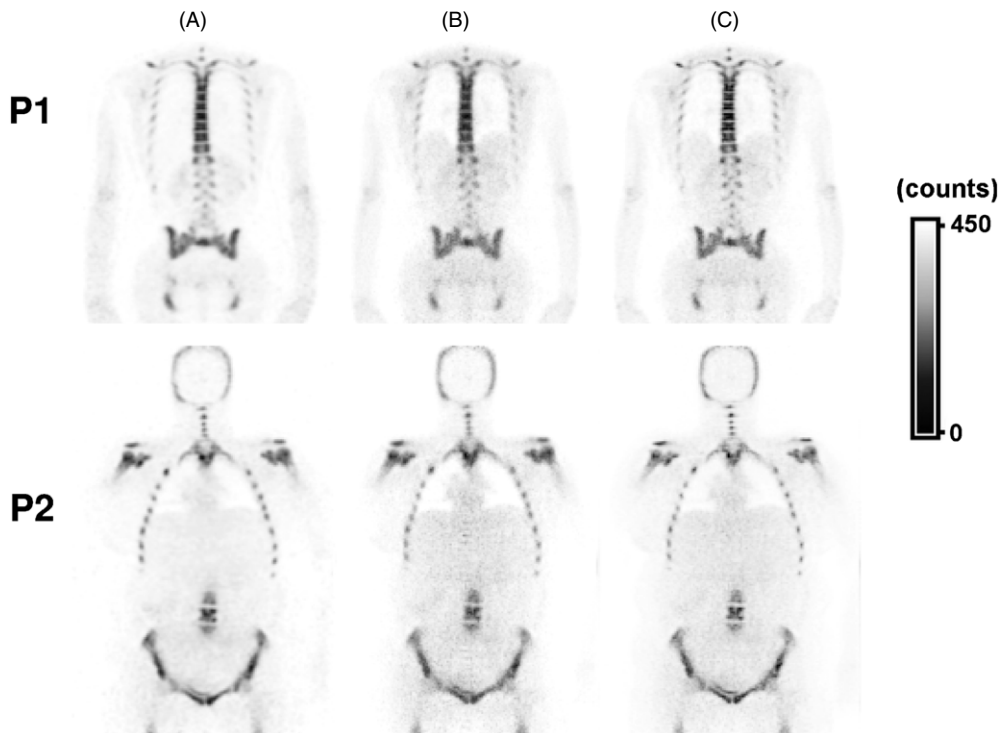

Figure 7. Coronal PET images from P1 (top) and P2 (bottom), and from LOR-RAMLA (A), M_{GEOM} (B) and M_{CRF} (C).

models the image point spread function. Figure 8 shows the 511 keV attenuation maps of the two patients and the ROIs used to draw the intensity profiles from images in figure 7. These profiles confirm that M_{CRF} gives higher resolution than the other methods.

Table 2 gives the computing times required for the different patient reconstructions, considering the 19 bed positions. The LOR-RAMLA reconstruction was performed on 3.60 GHz Xeon processors (using 1 CPU of 2 cores) and our reconstructions were performed on 2.27 GHz Xeon processors (using 10 CPUs of 8 cores). Times are given as if a reconstruction was performed using only one CPU (meaning one core of a processor), and included all iterations needed to obtain the images shown in figure 7 (see section 2.4).
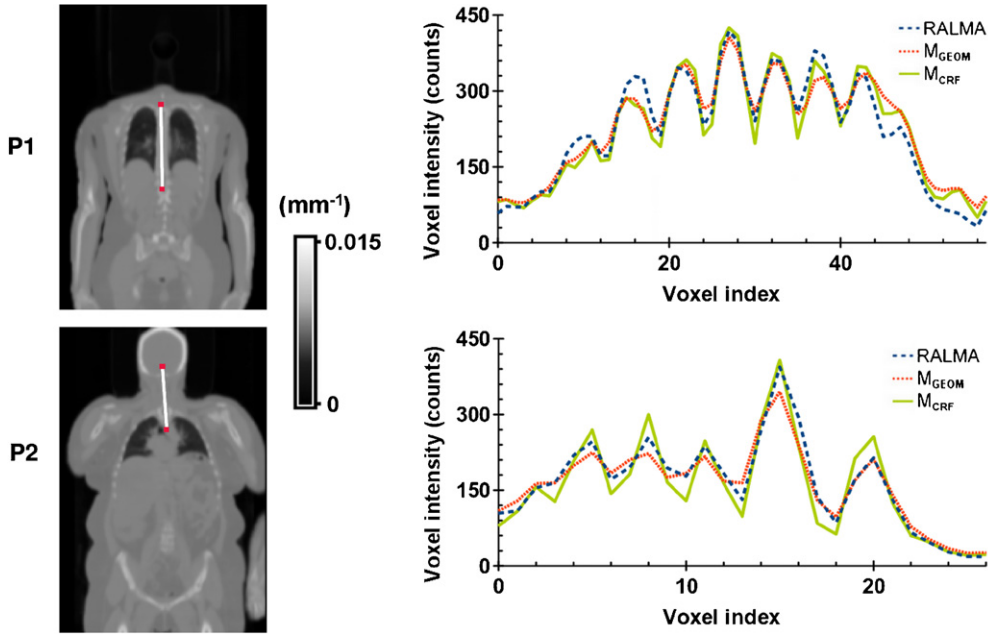
Figure 8. Data from P1 (top) and P2 (bottom). Left: 511 keV attenuation maps. Right: profiles plotted for each patient and for the three PET images (in figure 7), along the lines drawn in the 511 keV attenuation maps.

Table 2. Computing times for the different patient reconstructions.

Patient	LOR-RAMLA (s)	M_{GEOM} (s)	M_{CRF} (s)
P1	4785	8555	55 500
P2	8410	8690	55 200

4. Discussion

It is known that accurate modelling of various sources of blurring during reconstruction can improve the spatial resolution in the reconstructed images. Unlike most of the previous studies reporting CRF modelling using various strategies, here, by performing reconstructions in the LORH space, we distinguished between the intraC and interC effects in the CRF (figure 2), and considered resolution blurring effects along all dimensions. Modelling these effects improved resolution and CR, and each component had a significant effect. Moehrs *et al* (2008) have proposed a similar approach by considering two CRF components. They distinguished between scatter effects that occur between crystals (determined by Monte Carlo simulations), and penetration effects that occur inside crystals (determined by analytical considerations). However, scatter and penetration can actually both occur within or between crystals. In our work, we considered the combination of the two effects both within and between crystals, based on Monte Carlo simulations.

When modelling the two components simultaneously, spatial resolution and CR were further improved, and most important, we obtained an isotropic stationary resolution inside the FOV of ~4.2 mm FWHM (figure 2), close to the voxel size. The resolution values shown here do not reflect the actual resolution observed in clinical conditions, as well demonstrated and discussed by Alessio *et al* (2010). Still, they make it possible to precisely characterize

the improvement in resolution brought by each of the interC and intraC components. We intentionally neglected light readout effects, photon-pair non-collinearity and positron range in the phantom simulations. Indeed, we wanted to only investigate the role of crystal scattering and penetration at the intra crystal and inter crystal levels. Introducing other resolution-degrading effects in these phantom simulations would have introduced confounding factors preventing a specific analysis of the crystal interactions.

When modelling only simple geometric effects using the Siddon algorithm as in M_{GEOM} (one ray per LOR), some image voxels are not crossed by any LOR when the voxel size becomes small. For the GEMINI GXL, this limit is about 3 mm for cubic voxels. The manufacturer actually offers reconstruction with 2 mm voxel size, filling the zero-voxel values using blob-basis functions. Other projection algorithms such as the ray-driven (Joseph 1983) or distance-driven (De Man and Basu 2004) algorithms could be used. However, when modelling the intraC effect, the LORH space is oversampled, and the Siddon algorithm remains the most appropriate algorithm for multi-ray approaches, giving the exact path of a ray in a voxel-based geometry, and avoiding any interpolation. This LORH space oversampling thus makes reconstruction with smaller voxels theoretically feasible without empirical interpolation. However, a new matrix must be calculated for each voxel size and its size increases as the voxel size decreases. We could not build SMs using voxel size smaller than 4 mm due to the current hardware capacities.

When building the interC and intraC kernels, we assumed that all blocks and each block's quarter were affected by identical interC effects. This was true for the simulations as dimensions and materials were strictly the same between crystals. In a real scanner, this assumption remains realistic as the tolerance on dimension and material compounds is small. Dead-times, crystal efficiency and PMT efficiency do not affect this assumption as they are compensated before or during reconstruction. Pile-up effects were accounted for in simulations and can be supposed to be the same anywhere in the scanner. Nevertheless, checking this assumption practically remains a challenge.

A second assumption is that all crystals had the same distribution of probability of interactions within the crystal. In our simulation, we found that crystals at the border of the blocks had different count distributions from central crystals of the blocks. The 3D shape of the distribution looked the same but signals were more often detected deeper in the crystals at the edge of a block than at the centre. We could refine the method by considering four intraC kernels: one for crystals not at the edge of a block, one for crystals on the transaxial border, one for crystals on the axial border and one for the crystals in the corner. Inside these four categories, count distribution changes are negligible.

The intraC and interC kernels were derived by considering the simulated singles. As a result, in a given kernel, incidence angles were averaged. This means that during reconstruction, for a LOR passing through the centre of the transaxial FOV, too many large incidence angles are considered when using these kernels. Inversely, for a LOR passing at the edge of the transaxial FOV, too many small incidence angles are considered. When building the kernels by considering single events (and thus averaging incidence angles), we used real PET/CT data of a patient as the input of the simulation performed to build these kernels, in order to get a realistic sampling of the incidence angle distribution. Ideally, a couple of intraC and interC kernels should be calculated for each crystal involved in the definition of a LOR to accurately consider the incidence angles. Considering the scanner geometry, 3058 transaxial positions leading to different incidence angles are possible, and 29 axially. Storing these kernels individually considering isotropic 1 mm sampling for intraC kernels and 9×9 interC kernels in double precision format would require roughly about 77 GB, which is still feasible. However, the simulation time needed to estimate smooth kernels would be huge and is beyond

what can be practically achieved with conventional computational resources. Still, taking the incidence angle into account would certainly result in even better image quality. If applied to a rotating scanner made of a few heads that only admit coincidences between facing heads, the number of different possible incidence angles would be dramatically reduced. This method would thus be feasible by rotating the projector, as done by Moehrs *et al* (2008). However, such rotations involve interpolations, that would introduce some additional blur in the image.

M_{CRF} matrix did not have the largest number of non-zero voxels (table 1). When the dimensions of the interC kernel increase, the image space covered by the rays traced from this kernel increases too. However, when increasing the dimensions of the intraC kernel, its physical size does not increase much. Thus combining a 3×3 interC kernel with the intraC kernel did not produce larger matrix size than just using a 5×5 interC kernel. In our study, we empirically sampled a crystal using 300 elements. We tried smaller crystal sampling, but did not observe any substantial improvement (results not shown). We were not able to consider broader interC kernels, either used alone (in M_{interC}) or coupled to the intraC kernel (in M_{CRF}). Indeed, the size of the corresponding system matrices made them impossible to handle considering our current computer resources.

In the clinical study, data from the patients were saved as sinograms on the scanner console. At this stage, a sinogram element can already contain multiple geometric LORs of the LORH space, due to azimuthal angular mashing. When converting the sinograms into LORH, such elements were equally distributed to all contributing LORs, destroying the Poisson noise nature. Also, this smoothing process somehow disturbed the CRF physical properties and better improvements should be expected by considering data without angular mashing. However this was not practically feasible with our scanner in clinical routine. On the other hand, real data are affected by light-readout effects, photon-pair non-collinearity and positron range, that were not modelled in our SM. This explained why the improvements in resolution were smaller than those observed on the simulated data. However, these patient studies were only part of this work as an illustration, i.e. to show that even modelling a small part of all resolution degrading effects could significantly improve image quality.

5. Conclusion and future work

A new approach for modelling the CRF (i.e. crystal penetration and scattering effects) in four dimensions has been proposed and integrated into an iterative reconstruction algorithm based on LORH. In Monte Carlo simulated data, this algorithm yielded an isotropic and space-invariant resolution for point sources in air, and resulted in a significantly improved CR for any given level of noise. ^{18}F-NaF bone scans were also reconstructed to illustrate the potential of such an algorithm in clinical conditions.

Further work will consist in developing methods to compress the SM so that finer CRF modelling becomes achievable. Also, light readout effects will be incorporated into our model with an approach similar to that used to model the interC component. Photon-pair non-collinearity and positron range effects will be introduced separately as image-space sources of blur, thus depending on the patient/object scanned. These extensions will allow us to investigate the limits of such modelling techniques to improve the properties of reconstructed images.

Appendix. Details on the SM storage and reconstruction program

To store the SMs, the 4 492 872 calculated LORs were grouped by 1000 in 4500 separated files. The data arrangement is described in table A1.

Table A1. Data arrangement for a LOR stored on the hard disk drive or in RAM.

Description of the data	Type of data	Size in memory (Bytes)
Number of symmetries (S)	Unsigned short int	2
Index of symmetrical LORs	Unsigned int	$S \times 4$
Number of non-zero voxels (V)	Unsigned short int	2
Index of the voxels	Unsigned int	$V \times 4$
Probability of the voxels	Float simple precision	$V \times 4$

The reconstruction program was written in C++ and run under a Linux system. It was parallelized using the open-source OpenMPI[3] library to distribute the calculation on multiple computers. Each computer reads its own part of the SM to fully load it in RAM. Multi-threading using the open-source Boost library[4] was used to further parallelize the code execution on each computer, and to take advantage of direct SM memory sharing. The code was run on ten computers, each composed of two Intel Xeon 2.66 GHz quad-core processors and 24 GB of RAM.

Considering M_{GEOM}, the computation using eight threads of a single computer where the SM elements are calculated on-the-fly (OTF) is more than 20 times slower than when using pre-calculated M_{GEOM}. Considering M_{intraC}, M_{interC} or M_{CRF}, the matrices were too large for the reconstruction to be performed on a single computer. However for the same total number of calculation threads, computation time performing OTF reconstruction was about twice as slow as that for M_{intraC}. Overall, OTF reconstruction was about twice as fast as for M_{interC} or M_{CRF}. Time-comparison factors are given for the program to perform a complete MLEM iteration (i.e. without subset) and with all LORs different from 0; thus, no time for data transfer between threads and/or computers, nor image update, is needed.

References

Accorsi R, Adam L E, Werner M E and Karp J S 2004 Optimization of a fully 3D single scatter simulation algorithm for 3D PET *Phys. Med. Biol.* **49** 2577–98

Alessio A, Kinahan P and Lewellen T 2006 Modelling and incorporation of system response functions in 3D whole body PET *IEEE Trans. Med. Imaging* **25** 828–37

Alessio A M, Stearns C W, Tong S, Ross S G, Kohlmyer S, Ganin A and Kinahan P E 2010 Application and evaluation of a measured spatially variant system model for PET image reconstruction *IEEE Trans. Med. Imaging* **29** 938–49

Bailey D L and Meikle S R 1994 A convolution-subtraction scatter correction method for 3D PET *Phys. Med. Biol.* **39** 411–24

De Man B and Basu S 2004 Distance-driven projection and backprojection in three dimensions *Phys. Med. Biol.* **49** 2463–75

Holdsworth C H, Levin C S, Janecek M, Dahlbom M and Hoffman E J 2002 Performance analysis of an improved 3D PET Monte Carlo simulation and scatter correction *IEEE Trans. Nucl. Sci.* **49** 83–9

Hu Z *et al* 2007 An LOR-based fully-3D PET image reconstruction using a blob-basis function *IEEE Nucl. Sci. Symp. Conf. Rec.* **6** 4415–8

Jacobs F, Sundermann E, De Sutter B, Christiaens M and Lemahieu I 1998 A fast algorithm to calculate the exact radiological path through a pixel or voxel space *J. Comput. Inf. Technol.* **6** 89–94

Jan S *et al* for the OpenGATE collaboration 2004 GATE: a simulation toolkit for PET and SPECT *Phys. Med. Biol.* **49** 4543–61

Johnson C A, Yan Y, Carson R E, Martino R L and Daube-Witherspoon M E 1995 A system for the 3D reconstruction of retracted-septa PET data using the EM algorithm *IEEE Trans. Nucl. Sci.* **42** 1223–7

---

3 OpenMPI: Open Source High Performance Computing – www.open-mpi.org.
4 Boost: Boost C++ libraries – www.boost.org.

Joseph P 1983 An improved algorithm for reprojecting rays through pixel images *IEEE Trans. Med. Imaging* **1** 192–6

Kadrmas D J 2004 LOR-OSEM: statistical PET reconstruction from raw line-of-response histograms *Phys. Med. Biol.* **49** 4731–44

Lamare F, Turzo A, Bizais Y, Cheze Le Rest C and Visvikis D 2006 Validation of a Monte Carlo simulation of the Philips Allegro/GEMINI PET systems using GATE *Phys. Med. Biol.* **51** 943–62

Michel C, Sibomana M, Boi A, Bernard X, Lonneux M, Defrise M, Comtat C, Kinahan P E and Townsend D W 1998 Preserving Poisson characteristics of PET data with weighted OSEM reconstruction *IEEE Nucl. Sci. Symp. Conf. Rec.* **2** 1323–9

Moehrs S, Defrise M, Belcari N, Del Guerra A, Bartoli A, Fabbri S and Zanetti G 2008 Multi-ray-based system matrix generation for 3D PET reconstruction *Phys. Med. Biol.* **53** 6925–45

Mumcuoglu E U, Leahy R M, Cherry S R and Hoffman E 1996 Accurate geometric and physical response modelling for statistical image reconstruction in high resolution PET *IEEE Nucl. Sci. Symp. Conf. Rec.* **3** 1569–73

Ortuño J E, Kontaxakis G, Rubio J L, Guerra P and Santos A 2010 Efficient methodologies for system matrix modelling in iterative image reconstruction for rotating high-resolution PET *Phys. Med. Biol.* **55** 1833–61

Panin V Y, Kehren F, Michel C and Casey M 2006 Fully 3D PET reconstruction with system matrix derived from point source measurements *IEEE Trans. Med. Imaging* **25** 907–21

Politte D G and Snyder D L 1991 Corrections for accidental coincidences and attenuation in maximum-likelihood image reconstruction for positron-emission tomography *IEEE Trans. Med. Imaging* **10** 82–9

Qi J, Leahy R M, Cherry S R, Chatziioannou A and Farquhar T H 1998 High-resolution 3D Bayesian image reconstruction using the microPET small-animal scanner *Phys. Med. Biol.* **43** 1001–13

Rafecas M, Mosler B, Dietz M, Pögl M, Stamatakis A and McElroy D P 2004 Use of a Monte Carlo-based probability matrix for 3D iterative reconstruction of MADPET-II data *IEEE Trans. Nucl. Sci.* **51** 2597–605

Rahmim A, Tang J, Lodge M A, Lashkari S, Ay M R, Lautamäki R, Tsui B M W and Bengel F M 2008 Analytic system matrix resolution modeling in PET: an application to Rb-82 cardiac imaging *Phys. Med. Biol.* **53** 5947–65

Reader A J, Julyan P, Williams H, Hastings D and Zweit J 2003 EM algorithm system modeling by image-space techniques for PET reconstruction *IEEE Trans. Nucl. Sci.* **50** 1392–7

Selivanov V V, Picard Y, Cadorette J, Rodrigue S and Lecomte R 2000 Detector response models for statistical iterative image reconstruction in high resolution PET *IEEE Trans. Nucl. Sci.* **47** 1168–75

Siddon R 1985 Fast calculation of the exact radiological path for a three-dimensional CT array *Med. Phys.* **12** 252–5

Sureau F C, Reader A J, Comtat C, Leroy C, Ribeiro M J, Buvat I and Trébossen R 2008 Impact of image-space resolution modeling for studies with the high-resolution research tomograph *J. Nucl. Med.* **49** 1000–8

Tohme M and Qi J 2009 Iterative image reconstruction for positron emission tomography based on a detector response function estimated from point source measurements *Phys. Med. Biol.* **54** 3709–25

Veklerov E, Llacer J and Hoffman E J 1988 MLE reconstruction of a brain phantom using a Monte Carlo transition matrix and a statistical stopping rule *IEEE Trans. Nucl. Sci.* **35** 603–7

Yamaya T *et al* 2005 Transaxial system models for jPET-D4 image reconstruction *Phys. Med. Biol.* **50** 5339–55